# AERODYNAMIC STABILITY ANALYSIS OF A CUBESAT IN HIGH-SPEED RAREFIED FLOW

BY

JAMES WILLIAMS

THESIS

Submitted in partial fulfillment of the requirements
for the degree of Master of Science in Aerospace Engineering
in the Graduate College of the
University of Illinois at Urbana-Champaign, 2018

Urbana, Illinois

Advisor:
Assistant Professor Zachary Putnam

# Abstract

Small satellites, such as CubeSats and SmallSats, are seeing increased use in Low Earth Orbit, particularly at altitudes with measurable aerodynamic effects. It is important to design these spacecraft, which often have modest control authority, such that the resultant aerodynamic forces and moments do not cause unstable motion, which may lead to premature loss of mission. Building from free molecular pressure and shear equations for flat plates, an aerodynamic solver is designed to analyze the aerodynamic forces and moments on a 3U CubeSat with center of gravity offset, orbiting at altitudes from 80 to 200 km. The motion of this CubeSat is then simulated for a variety of initial conditions, both with and without active control, to determine its behavior. Inferences are made as to design rules that will lead to more stable small satellites.

*To my mother, father, sister, and brother, whose constant encouragement and help allowed me to achieve more than I ever thought possible.*

# Table of Contents

# Chapter 1

# Introduction

The Karman line, which is the canonical boundary between Earth's atmosphere and space, lies 100 km above sea level[1]. In reality, the atmosphere extends much further. Above 100 km altitude, the atmosphere exists as an extremely rarefied collection of molecules [2]. Space vehicles interacting with this region of the atmosphere experience measurable aerodynamic forces and torques. For SmallSat and CubeSat missions which often have small, if any, $\Delta$v budgets and modest attitude control authority, these aerodynamic affects can cause issues for mission lifetime and effectiveness. It is desirable to investigate the effects of aerodynamic forces on these smaller missions to allow mission planners better ability to predict the longevity and performance of their vehicles in Low Earth Orbit (LEO).

Of particular interest is the aerodynamic stability of CubeSats. As the orbit of a CubeSat degrades due to atmospheric drag, the aerodynamic torques on the spacecraft may begin to overpower the modest attitude control system onboard. Thus, the spacecraft may be required to make a switch from active to passive control: At a certain altitude, the spacecraft must be in a nose-forward orientation with enough center of gravity (cg) offset to allow it to maintain orientation as the aerodynamic forces grow greater. This is demonstrated in Figure 1.1.

Within the category of CubeSats, this work is quite useful for low-cost atmospheric probe missions intending to use CubeSat and SmallSat technology, like the upcoming Student Aerothermal Spectrometer Satellite of Illinois and Indiana (SASSI$^2$)[3] and Qubesat for Aerothermodynamic Research and Measurement on AblatioN (QARMAN)[4]. This style of mission depends heavily on the aerodynamic properties of these small vehicles. In the case of SASSI$^2$, the mission's duration and quality of data both rely on the pointing accuracy of the nose-forward orientation [5]. This places a great importance on the pointing capability of the spacecraft, especially during the portions of the mission with larger-magnitude aerodynamics.

Much of the previous work devoted to aerodynamics at altitudes relevant to orbit has been devoted to drag models for predicting rates of orbital degradation [6]. Some previous analysis has been performed on the rigid-body dynamics of slender bodies in free-molecular flow [7] and generic shapes in transition flow immediately before entry [8], but there has been limited if any inspection of the rigid-body dynamics and

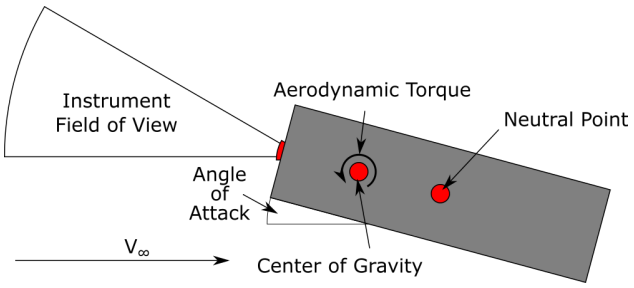


Figure 1.1: Graphical introduction to the problem: A CubeSat acting as an atmospheric probe should be designed such that it is aerodynamically stable.

stability of bluff bodies in orbit around Earth.

This work describes the development of a CubeSat aerodynamics solver which uses free-molecular pressure and shear equations to determine the aerodynamic forces and moments on a 3-U CubeSat. Using the assumption of hypersonic shadowing, the spacecraft is modeled as three orthogonal flat plates. The torque of the spacecraft acts around the center of gravity, which is positioned in front of the neutral point. It is created by the differing areas on which the pressures and shear are acting, compounded by the different lengths of moment arm.

Further analysis covers the resultant dynamics of the CubeSat as it orbits in the rarefied atmosphere. A lack of appreciable viscous damping forces causes the CubeSat to oscillate around its trimmed condition with no signs of stopping. For this reason, controlled damping is considered, which assumes the CubeSat has a modest control authority, capable of providing a derivative control on the order of $1 \times 10^{-5}$ N-m.

From this analysis, inferences are made regarding the design of CubeSats and SmallSats for use as high-altitude atmospheric probes. In general, a further-fore center of gravity creates larger restoring torques, and thus a larger static margin, but also requires larger control magnitudes to damp the motion for similar time scales. Similarly, a more massive spacecraft requires larger control magnitudes than a less massive one of similar size.

# Chapter 2

# Methodology

## 2.1 Definition of Continuum, Transition, and Free-Molecular Flows

A flow may be categorized as either continuum, transitional, or free-molecular [9, 10, 11]. These categories depend on the mean free path, $\lambda$, of the gas, which is the mean distance between particle-particle collisions within the gas. A more useful metric for spacecraft analysis is the Knudsen number, $Kn$, which is the ratio of mean free path to the characteristic length of the vehicle. Common ranges for Knudsen numbers corresponding to different regimes of flight are shown in 2.1 [12].

Table 2.1: Common ranges of Knudsen number corresponding to regimes of flows

| Category | $Kn$ |
|---|---|
| Continuum | 0.001 — 0.01 |
| Transitional | 0.01 — 10 |
| Free-molecular | >10 |

At 150 km altitude, $\lambda$ is roughly 150 m. For a CubeSat with a characteristic length of 0.1 m, this leads to a $Kn$ of 1500, well within the range of free-molecular flight. Thus, any investigation into the aerodynamics of vehicles in low-LEO must use equations which take into account free-molecular assumptions.

## 2.2 Comparison of Existing Rarefied Aerodynamic Methods

Currently, there are a few aerodynamics analysis methods available to mission planners intending to operate satellites in low-LEO. Of note among these are low-fidelity models used primarily for drag calculations, and high-fidelity models which are computationally expensive.

Low-fidelity free-molecular aerodynamics solvers, such as those found in the General Mission Analysis Tool (GMAT) [13] and the Systems Tool Kit (STK) [14], are primarily used to determine the amount of atmospheric drag on a spacecraft and how this drag affects the time-evolution orbit of the spacecraft. To

this end, the most common method is to generate a drag model based on a spherical approximation of the spacecraft, a corresponding area/mass ratio, and a corresponding drag coefficient. This form of aerodynamic modeling does not natively support functionality to determine the aerodynamic torques on the spacecraft resulting in attitude changes.

High-fidelity modeling of rarefied flows often takes the form of direct-simulation Monte Carlo (DSMC) solvers, which stochastically determine flow properties around a body. Time-accurate solvers such as the Stochastic PArallel Rarefied-gas Time-accurate Analyzer (SPARTA) [15] are able to determine the pressures on individual faces of a body, which allows for the calculation of torques around the center of gravity. The drawbacks to this method of analysis are the large computational cost associated with the simulation, the difficulty in setting up the problem and validating results, and the large base of knowledge required to effectively run the simulations.

## 2.3 Free-molecular Aerodynamics

Analytical expressions have been developed for the flow over various shapes in free-molecular flow, as described by Schaaf and Chambre (S&C) [16]. Of particular interest to this work are the equations of pressure, $p$, and shear, $\tau$, relating to flat plates, as these can be superimposed to approximate any other shape. These equations are

$$\begin{aligned} p = \frac{\rho U^2}{2S^2}\Big[\Big(\frac{2-\sigma'}{\sqrt{\pi}} S\sin\theta + \frac{\sigma'}{2}\sqrt{\frac{T_w}{T}}\Big)e^{-(S\sin\theta)^2} \\ + \Big\{(2-\sigma')[(S\sin\theta)^2 + \frac{1}{2}] \\ + \frac{\sigma'}{2}\sqrt{\frac{\pi T_W}{T}}(S\sin\theta)\Big\}[1+\mathrm{erf}(S\sin\theta)]\Big] \end{aligned}$$

$$\tau = -\frac{\sigma\rho_\infty U^2\cos\theta}{2\sqrt{\pi}S}\{e^{-(S\sin\theta)^2} + \sqrt{\pi}(S\sin\theta)[1+\mathrm{erf}(S\sin\theta)]\}$$

$$S = \frac{U}{\sqrt{2RT}} = \frac{\gamma}{2}M$$

where $\rho$ is the mass density of the flow, $U$ is the flow speed, $\sigma'$ and $\sigma$ are the accomodation coefficients for the material moving through the flow, S is the speed ratio, $R$ is the gas constant, $\theta$ is the impact angle measured from parallel, and $T_w$ and $T$ are the wall and freestream temperatures, respectively.

This formulation of the pressure and shear follow multiple assumptions. Because this work does not include the aerothermodynamics of the CubeSat as it is moving through the free-molecular flow, $T_w$ is assumed to equal $T$ [17]. The accommodation coefficients, $\sigma$ and $\sigma'$, are considered to be 0.9 [18].

These analytical expressions can express the pressure and shear of a flat plate at any angle relative to the flow. To confirm the accuracy of the equations, their results were compared to experimental work performed by Koppenwallner [17]. The results from this are shown in Table 2.2, and show strong agreement between the two bounding cases. The parallel plate case is a flat plate arranged with its long side parallel to the flow, creating drag solely from shear effects. The perpendicular disk case is a flat plate arranged with its long side perpendicular to the flow, creating drag solely from normal pressure.

Table 2.2: Coefficient of drag for flat plates and disks from theory (S&C) and experiment (Koppenwallner).

| **Category** | **S&C** | **Koppenwallner (Equation)** | **Koppenwallner (Experiment)** |
|---|---|---|---|
| Parallel Plate | 0.0337 | 0.0337 | 0.03 |
| Perpendicular Disk | 2.957 | 2.957 | 3.0 |

Table 2.3: Flight conditions for S&C comparison with Koppenwallner

| **Mach Number** | **Equivalent Altitude** | **Accommodation Coefficients** |
|---|---|---|
| 20 | 150 km | 1 |
| **Gas** | **Ratio of Specific Heats** | **Wall Temperature (Stagnation)** |
| Air | 1.4 | $5.7 \times 10^4$ K |

Additional comparisons were made between SPARTA and the S&C expressions, as shown in Table 2.4. The flight conditions for this comparison are shown in Table 2.5. Overall, there is a strong agreement between the two methods. The largest percent differences arise from areas with minimal magnitude of pressure and shear, which therefore have a small net effect on the overall forces experienced by the vehicle.

## 2.4 CubeSat Aerodynamics

Figure 2.1 shows the side view of the CubeSat analyzed in this work. The normal and shear pressures integrate over each face to produce forces. These forces then act around the center of gravity, producing a

Table 2.4: Pressure and Shear values from S&C and DSMC

| | S&C | DSMC | % Difference |
|---|---|---|---|
| **Normal Pressure (Front, Pa)** | 0.206 | 0.207 | 0.48 |
| **Shear Pressure (Front, Pa)** | 0.0143 | 0.0106 | 30 |
| **Normal Pressure (Top, Pa)** | 0.0024 | 0.00118 | 68 |
| **Shear Pressure (Top, Pa)** | 0.0143 | 0.0103 | 33 |
| **Normal Pressure (Side, Pa)** | 2.79e-04 | 0.00 | N/A |
| **Shear Pressure (Side, Pa)** | 0.0027 | 0.002717 | 0.63 |
| **Total drag pressure (Pa)** | 0.24 | 0.23 | 3.5 |

Table 2.5: Flight conditions for S&C comparison with SPARTA

| **Velocity** | **Equivalent Altitude** | **Accommodation Coefficients** | **Wall Temperature** |
|---|---|---|---|
| 8000 m/s | 150 km | 0.9 | 300 K |
| **Gas** | **Ratio of Specific Heats** | **Angle of Attack** | **Sideslip Angle** |
| Argon | 1.66 | -5$^o$ | 0$^o$ |

torque. The shadowed region in the image is an artifact of the hypersonic assumptions inherent to the analysis [19]. Because the vehicle is moving so fast through the rarefied atmosphere, the area immediately behind it is functionally a vacuum, and thus provides no contribution to the pressures acting on the spacecraft.

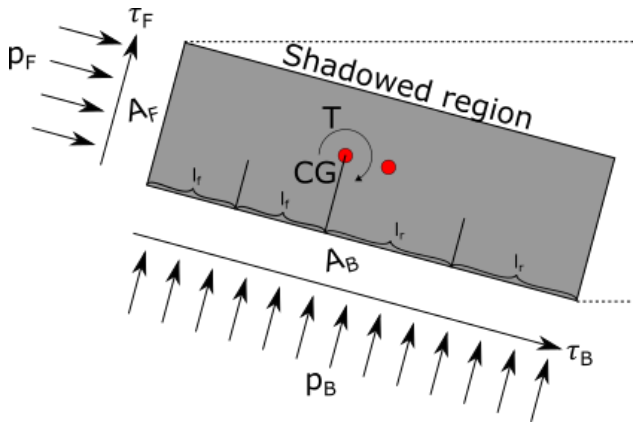


Figure 2.1: Sideview of CubeSat showing the normal and shear pressures acting on the spacecraft, as well as the resultant torque about the center of gravity (cg). Not shown: pressures on side face.

This shadowed region allows this CubeSat to be approximated as only three flat plates: A front/back plate, top/bottom plate, and left/right side plate. In trimmed flight, the front of the CubeSat is exposed to the flow, while the back plate is completely covered. Additionally for this case, the top/bottom and left/right side plates are in equilibrium which cancels out any resultant forces or moments arising from them. As the CubeSat pitches upward from trim it exposes the bottom plate to the flow while shadowing the top, and vice

versa if it pitches downward from trim. This work has only concerned itself with the 1-dimensional rotation of the spacecraft about its pitch axis, so the left/right side plates are always in their equilibrium state.

The position of the center of gravity (cg) has great importance on the stability of a vehicle due to the slope of the pitching-moment curve, as shown in Figure 2.2. In general, a negative slope of pitching moment coefficient with respect to angle of attack indicates a stable configuration [20]. As the vehicle pitches upward (positive angle of attack) a negative torque is produced, causing the vehicle to pitch back down. The inverse is true of a positive slope – an upward pitch creates a positive torque which further pitches the spacecraft upward.

To create a negative sloping pitching moment curve, the cg must be placed fore of the neutral point, which is the point on the vehicle around which all aerodynamic moments sum to zero. For the CubeSat case, the neutral point is located at the geometric center of the spacecraft.

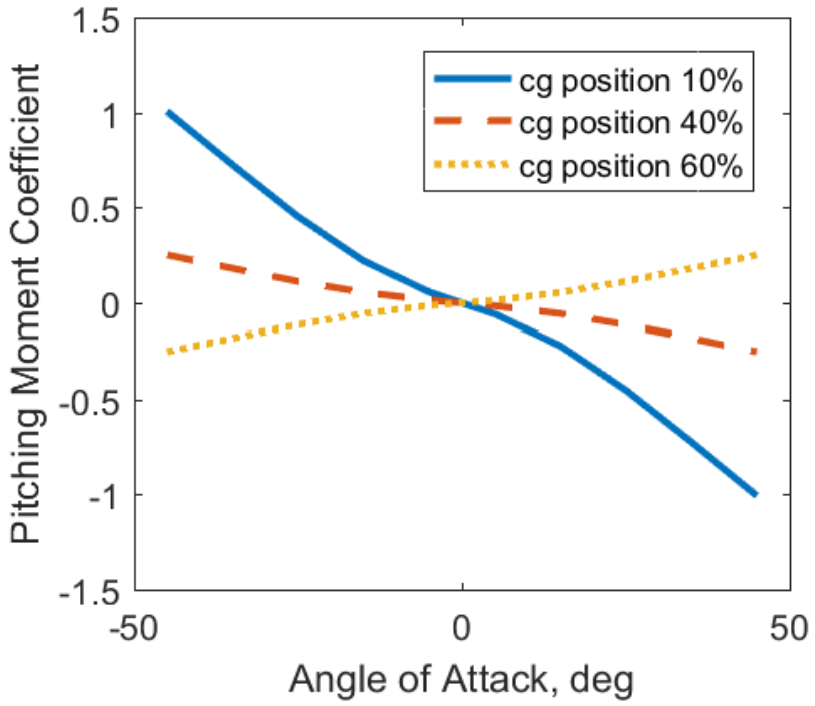


Figure 2.2: Pitching moment coefficient vs. angle of attack for various cg positions

An intuitive explanation for the effects of the cg position on the stability of the spacecraft can be made using a single flat plate. Figure 2.3 shows a flat plate with cg offset toward the front of the spacecraft . The total force on the fore and aft sections is a function of the pressures, which are the same across the entire flat plate, and the areas, which are unequal. For this case, the force fore of the cg is smaller than that aft of the cg. Similarly, the moment arm about which the force produces a torque is different for the fore and aft

cases. The larger aft force produces a large negative torque, while the smaller fore force produces a smaller positive torque. The net result is a negative torque for a positive angle of attack. The net torque modeled on the vehicle is described by

$$T_{aero} = \text{sgn}(\alpha)\Big[\frac{{cg_x}^2}{2L}p_B A_B - \frac{(L-cg_x)^2}{2L}p_B A_B + cg_x \tau_F A_F - cg_y \tau_B A_B\Big]$$

where $T_{aero}$ is the aerodynamic torque in the pitch axis, $\text{sgn}(\alpha)$ is the sign of the angle of attack, $cg_x$ is the distance between the front plate and the center of gravity, $cg_y$ is the distance between the bottom plate and the center of gravity, $L$ is the overall length of the spacecraft, $p_B$ is the normal pressure on the bottom of the spacecraft, $\tau_F$ is the shear pressure on the front of the spacecraft, and $\tau_B$ is the shear pressure on the bottom of the spacecraft.

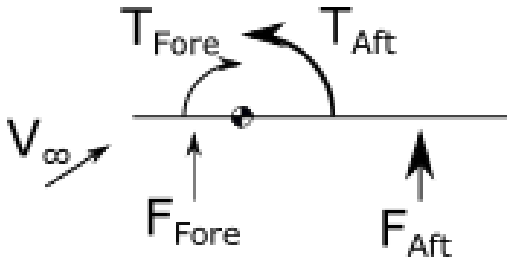


Figure 2.3: Demonstration of relative torques arising from cg offset.

## 2.5 Moment of Inertia & Center of Gravity

The moment of inertia (MOI) of a vehicle describes how resistant it is to rotational accelerations, and is therefore an important parameter in stablity analysis. The development of the MOI for a physical vehicle is determined by the position of each component within the vehicle, and is beyond the scope of this work. A more simple model is instead used in which a point mass of variable mass is modeled in the nose of the vehicle, which is modeled as a solid rectangular prism. The derivation is as follows

$$m_{pt} = m_{tot}(1 - 2\frac{x}{L})$$

$$m_{rect} = m_{tot} - m_{pt}$$

$$I_{pt} = m_{pt}\Big(\frac{L}{2}\Big)^2$$

$$I_{rect} = m_{rect}\frac{(L^2+H^2)}{12} + m_{rect}\Big(L(\frac{1}{2} - \frac{x}{L})\Big)^2$$

$$I_{yy} = I_{rect} + I_{pt}$$

where $m_{pt}$ is the mass of the point in the nose of the vehicle, $x$ is the position of the cg measured from the nose, $m_{tot}$ is the total mass of the vehicle, $m_{rect}$ is the mass of the rectangular prism, $L$ is the length of the vehicle, $H$ is the height of the vehicle, $I_{pt}$ is the moment of inertia of the point mass measured from the cg, $I_{rect}$ is the moment of inertia of the rectangular prism measured from the cg using the parallel axis theorem, and $I_{yy}$ is the total moment of inertia of the system.

The mass of the point mass/prism pair is held constant while the relative masses are changed to accommodate different MOIs and cg positions. Figure 2.4 shows the dependence on the MOI on the the cg position. A cg closer to the neutral point has the effect of decreasing the MOI.

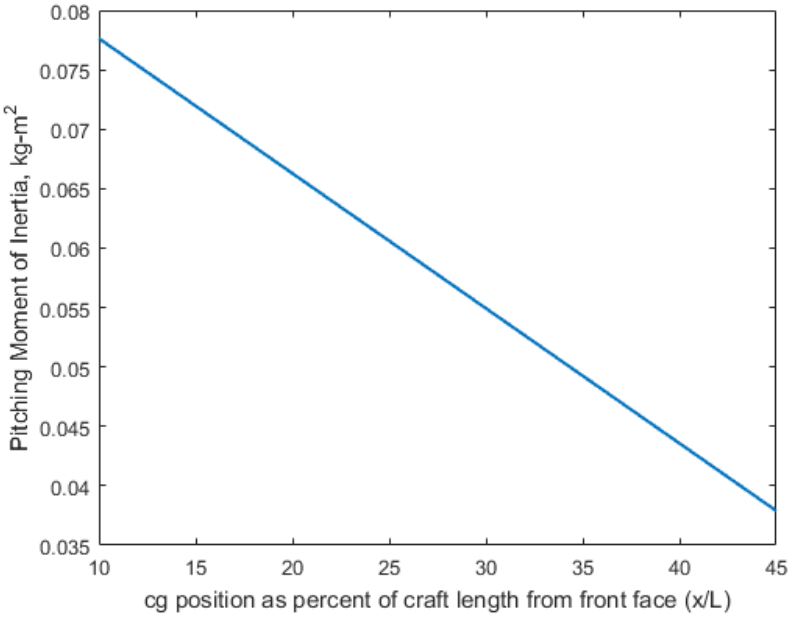


Figure 2.4: Moment of Inertia vs. cg position for a 3U CubeSat

## 2.6 Atmospheric Models

This work uses the MSIS-E-90 (Mass Spectrometer and Incoherent Scatter Radar - Exosphere) Atmosphere Model to simulate the conditions of the atmosphere at altitude[21]. This model is able to estimate the total mass density, neutral temperature, and individual molecule number density as a function of altitude between 0 and 1,000 km. For this work, the mass density and neutral temperatures were queried for the date of January 1, 2000, as shown in Figure 2.5

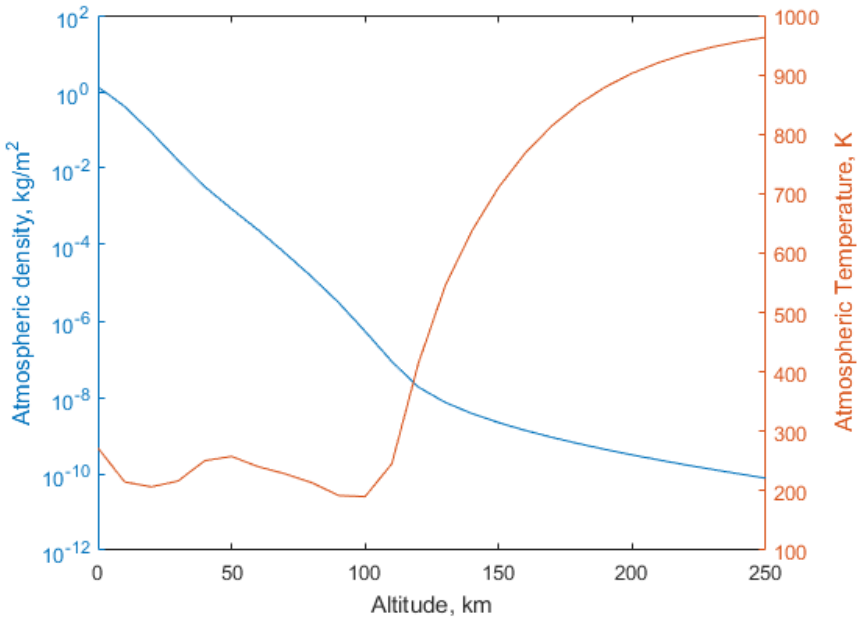


Figure 2.5: Atmospheric density and neutral temperature vs. altitude based on MSIS-E-90

## 2.7 Attitude Dynamic Simulation

The CubeSat is modeled as three orthogonal flat plates arranged around a center of gravity, orbiting around the Earth in an inverse-square gravity field. The simulations are circular orbits between altitudes of 80 km and 200 km.

The state of the CubeSat is the $13 \times 1$ vector

$$[\mathbf{Y}]^T = [\mathbf{r}^T, \mathbf{v}^T, q_0, q^T, \omega^T]$$

with the dynamics modeled for the CubeSat described by the $13 \times 1$ vector

$$[\dot{\mathbf{Y}}] = \begin{bmatrix} \dot{\mathbf{r}} \\ \dot{\mathbf{v}} \\ \dot{q_0} \\ \dot{\mathbf{q}} \\ \omega \end{bmatrix} = \begin{bmatrix} \mathbf{v} \\ -\frac{-\mu \mathbf{r}}{r^3} \\ \frac{1}{2}\omega^T q_0 \\ \frac{1}{2}(\omega q_0 - \widehat{\omega}\mathbf{q}) \\ I^{-1}\tau - I^{-1}\widehat{\omega} I \omega \end{bmatrix}$$

where $\mathbf{r}$ is the radius vector in inertial space, $r$ is the magnitude of the radius vector, $\mathbf{v}$ is the velocity vector in inertial space, $\mu$ is the gravitational parameter of Earth, $q_0$ and $q$ form the CubeSat's rotation quaternion $\mathbf{Q} = [q_0, \mathbf{q}]^T$, $\omega$ is the angular velocity of the CubeSat, and $I$ is the moment of inertia matrix for the CubeSat. The torque $\tau$ is a function of the aerodynamics of the vehicle and any onboard control used by the vehicle. The hat modifier over $\widehat{\omega}$ indicates the cross product matrix

$$\widehat{\omega} = \begin{bmatrix} 0 & -\omega_3 & \omega_2 \\ \omega_3 & 0 & \omega_1 \\ -\omega_2 & \omega_1 & 0 \end{bmatrix}$$

The aerodynamics of the vehicle depend on the vehicle's current angle of attack, $\alpha$, which is itself dependent on the vehicle's position, velocity, and attitude in inertial space. Multiple frames of reference are used to develop the body-fixed orientation of the vehicle [22, 23]. The basis of this analysis is an Earth-Centered Inertial (ECI) frame. A Local-Vertical-Local-Horizontal (LVLH) frame is then used to provide a reference for the flight path angle, $\gamma$, of the vehicle. The flight path angle is then used to develop a Wind frame which is rotated around the y-axis of the LVLH frame by $\gamma$. The body-fixed frame is found by sequentially rotating around the x, z, and y axes of the wind frame by the bank angle $\sigma$, sideslip $\beta$, and angle of attack $\alpha$, respectively.

The dynamics are then simulated using the Runge-Kutta 4 method based on initial conditions.

## 2.8 Anticipated Mission Profile

This work anticipates a mission profile consisting of multiple phases. The CubeSat will be deployed after a rideshare into a nearly-circular orbit of some altitude above the Earth. The CubeSat cannot be assumed to be in a nose-forward, trimmed attitude upon deployment. This is expressed in the simulation in 1-D as an initial angle of attack.

# Chapter 3

# Uncontrolled Motion of CubeSat

## 3.1 Lack of Aerodynamic Damping

Due to the high-speed, rarefied nature of the flow with which the vehicle is interacting, there is limited, if any, aerodynamic damping that occurs. Figure 3.1 shows the angle of attack versus time for conditions summarized in Table 3.1.

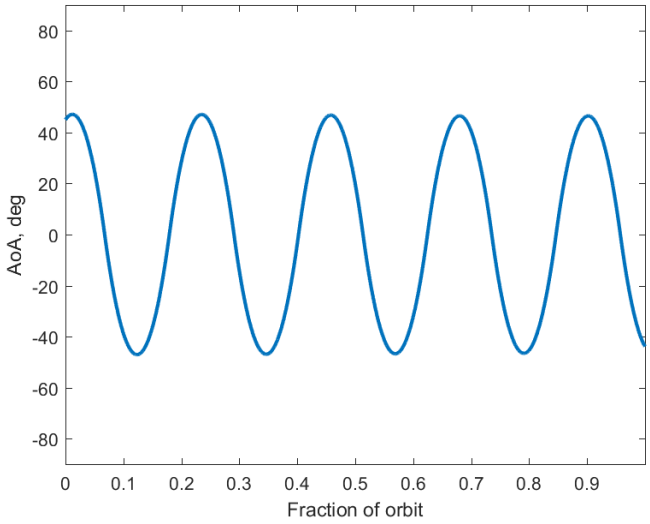


Figure 3.1: Angle of Attack vs. Fraction of Orbit for a vehicle with cg position of 30% spacecraft length, no control

Table 3.1: Conditions for simulation

| Altitude | $\alpha_0$ | $\dot{\alpha_0}$ | Cg position | Control |
|---|---|---|---|---|
| 150 km | $45^o$ | $0^o/s$ | 30% from nose | $k_d = k_p = 0$ |

The rarefied nature of the flow causes a lack of dissipative, viscous forces acting against the motion of the vehicle[7]. Similarly, the immense speed limits the relative angle of attack of the various portions of the vehicle, as shown in Figure 3.2 [12]. At a freestream velocity of 7.8 km/s, which corresponds to a circular

orbit of 150 km altitude, a pitch rate of $5^o$/s corresponds to an angle of attack difference between the nose and center of mass of roughly $6 \times 10^{-5}$ $^o$. Pitch rates much above $5^o$/s are difficult for CubeSat attitude determination and control (ADCS) systems to effectively manage.

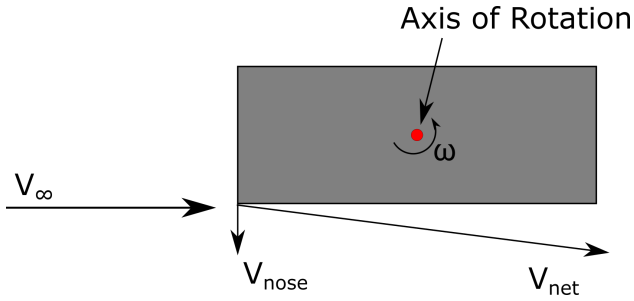


Figure 3.2: The rotation rate of the vehicle induces a relative velocity at the tips of the vehicle. This creates a miniscule difference in angle of attack.

## 3.2 Dependence on Altitude

The atmosphere becomes more dense as the vehicle descends, and the magnitude of the aerodynamic effects increases accordingly. Between 80 and 200 km altitude, the density of the atmosphere varies from $1.5 \times 10^{-5}$ kg/m$^2$ to $3.1 \times 10^{-10}$ kg/m$^2$, or a factor of nearly 46,000. Figure 3.3 shows the resultant frequency of oscillation for a CubeSat beginning at $45^o$ angle of attack. These cases are considered without the inclusion of control. As the spacecraft descends in the atmosphere, the density of the atmosphere increases and so does the magnitude of the restorative torque. This in turn has the effect of increasing the frequency of oscillation of the CubeSat around its trim point.

A curious artifact appears best in the 150 km and 200 km cases shown in Figure 3.4. At the beginning of the simulation, the vehicle is at an angle of attack of $45^o$ and a pitch rate of $0^o$/s relative to inertial space. As the orbital motion of the vehicle brings it around the Earth, it initially maintains its inertial orientation, but has a rotation rate relative to the horizon. This causes the effective angle of attack to increase, up to roughly $60^o$ in the case of the 200 km orbit. As the effect of the aerodynamic torque accelerates the vehicle into a spin, it effectively reaches a higher maximum angle of attack than it started at, causing it to maintain a higher amplitude of oscillation than initially assumed.

## 3.3 Dependence on Cg Position

A secondary inference from Figure 3.4 is the relation between cg position and the frequency of oscillation of the vehicle about its trim point. For the cases considered, cg position of 10% of the spacecraft length

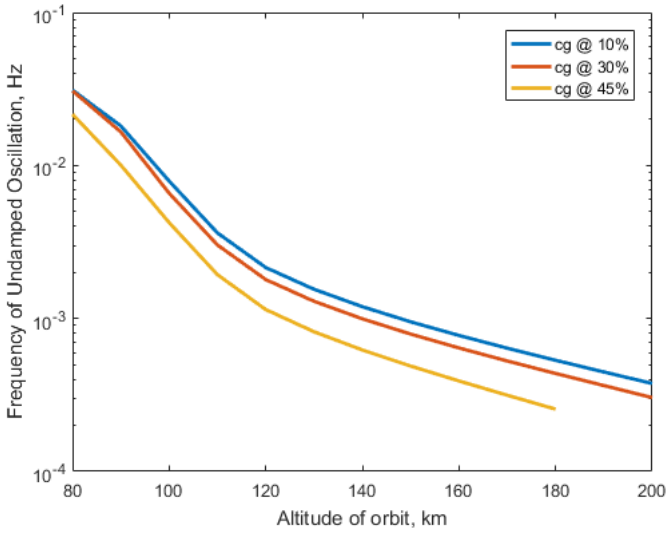


Figure 3.3: The effect of reduced altitude is a higher frequency of oscillation. $\alpha_0 = 45^o$.

produces the highest-frequency oscillations, while a cg position of 45% produces the lowest-frequency, and appears to have the same lagging effect as the high-altitude cases mentioned previously.

This work does not include analysis of a vehicle with cg at 50% of spacecraft length. This is due the difficulties related to modeling such a case. Because the torque calculated by the simulation of the vehicle is related to the offset of the cg from the neutral point, a case with cg coincident with neutral point leads to zero torque produced for any angle of attack, and thus a vehicle that maintains its initial state for the entire simulation. This is a nonphysical result: small disturbances in the flow would produce unpredictable torques on the spacecraft, causing it to tumble.

Figure 3.5 demonstrates the effect of placing the cg behind the neutral point. For a cg at 55% or 70% of the spacecraft length, the initial torque is positive, creating a rotational acceleration which pushes the vehicle further from $0^o$ angle of attack.

## 3.4 "Zero-Zero" performance

A simulation is considered in which the vehicle begins at $0^o$ angle of attack and $0^o$/s angle of attack rate. Figure 3.6 shows this case. As discussed before, there exists an induced angle of attack due to the orbital motion of the vehicle. In this case, the magnitude of the oscillations is roughly $12^o$ at 200 km altitude.

An important realization from this particular analysis is the fact that the oscillations produced by the natural motion of the vehicle may not require any active control to maintain. In the 150 km case, the amplitude of the oscillations from the zero-zero initial state is roughly $2^o$, which is within the pointing

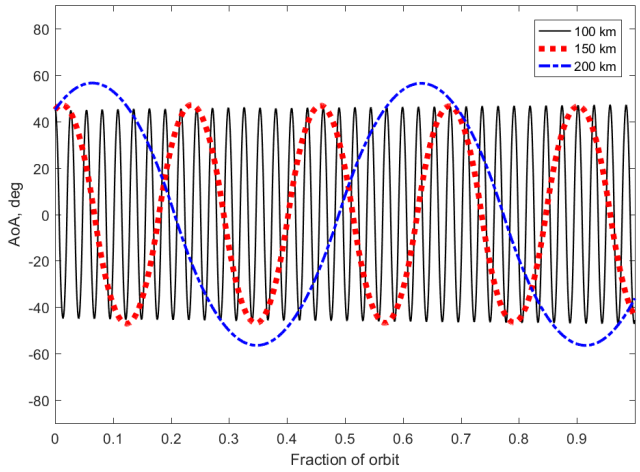


Figure 3.4: The effect of reduced altitude is a higher frequency of oscillation. $\alpha_0 = 45^o$.

requirements for some missions [3]. This implies that a vehicle only need trim itself to a small enough angle of attack magnitude and rate to maintain pointing requirements during the transit deeper into the atmosphere. If the vehicle is trimmed, its oscillations will not grow in magnitude beyond what they originate at.

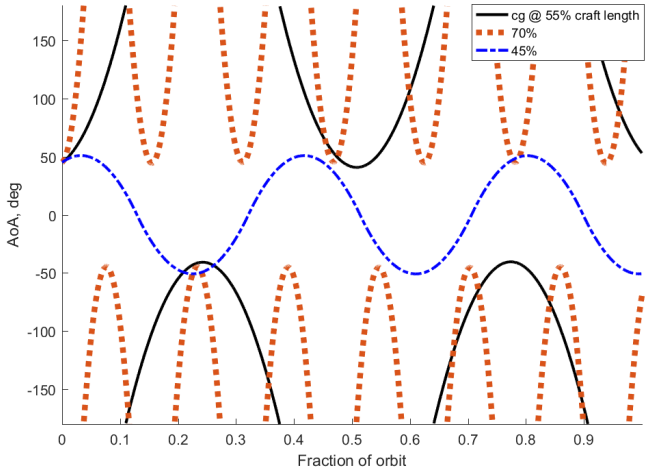


Figure 3.5: The effect of a cg placed behind the neutral point is to oscillate around $180^o$ angle of attack. $\alpha_0 = 45^o$, alt = 150 km.

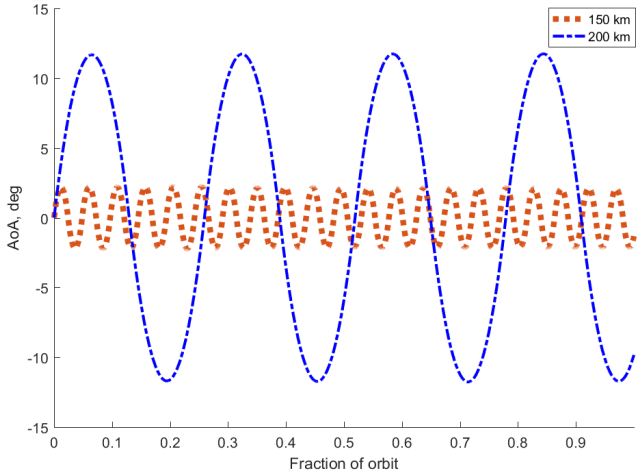


Figure 3.6: A vehicle beginning at $\alpha_0 = 0^o$ and $\dot{\alpha_0} = 0^o/s$. cg = 30%.

# Chapter 4

# Controlled Motion of CubeSat

## 4.1 Methods of Sensing and Control

Any closed-loop control of a system requires sensing to determine the required control input. For space vehicles, attitude determination can be performed by a wide variety of possible instruments, including inertial measurement units (IMUs), magnetometers, and star trackers[24]. For atmospheric probes, it is also possible to use a collection of pressure ports to determine the angle of attack of the vehicle relative to the flow [25]. CubeSats often do not have the mass, power, or budget available to use higher-end equipment such as star trackers. Instead, they are often equipped with IMUs and magnetometers, which are relatively inexpensive. The drawback of using an IMU is that it senses accelerations and integrates them to determine velocity and position, which may lead to inaccuracies in the anticipated values [26].

CubeSat attitude control often comes in the form of magnetorquers or reaction wheels. Magnetorquers are generally less expensive than reaction wheels, but rely on the Earth's magnetic field to operate, and have limitations on available torque magnitude and direction based on the CubeSat's position around the Earth. Reaction wheels have no such limitations, but are often bulky and expensive.

For this analysis, it was assumed that the CubeSat would be equipped with an IMU to measure body-fixed rotational rates and a set of pressure ports capable of rapidly determining angle of attack. Additionally, it was assumed that the CubeSat was equipped with a reaction wheel to perform control. Further analysis will be required to implement magnetorquing capability.

## 4.2 Active Control

While the onboard control of CubeSats and Smallsats is often too weak to affect considerable change at lower altitudes, it may still be used to provide rate damping to the motion of the vehicle. Figure 4.1 shows a case with the same initial conditions as Figure 3.1 but with the inclusion of control on the pitch axis of angular velocity. This effectively acts as a derivative controller on the angle of attack, damping the motion

over the course of the orbit.

It is important to note that the control used has been neither tuned nor optimized; the challenge of gain scheduling as a function of altitude is not the focus of this work. Additionally, this control assumes a maximum control effort of $1 \times 10^{-5}$ N-m of torque acting on the vehicle. This is approximately half of the maximum magnitude expected from the magnetorquing control system onboard the IlliniSat-2 Bus. The half-factor is a conservative assumption to account for the lack of useful control authority of the control system during portions of an inclined orbit.

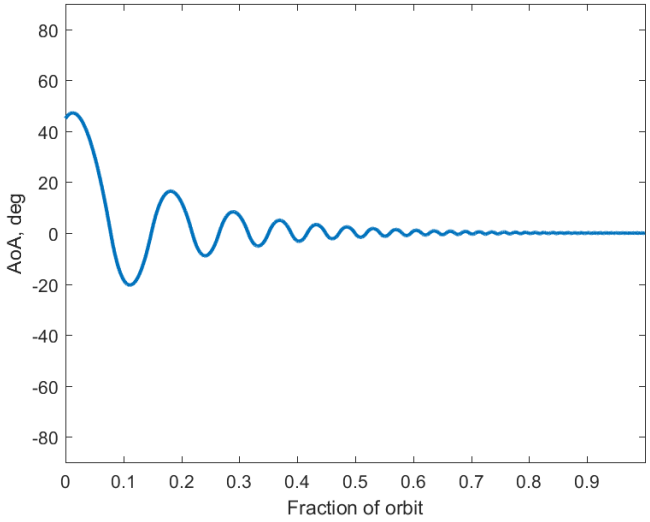


Figure 4.1: Angle of Attack vs. Fraction of Orbit for a vehicle with cg position of 30% spacecraft length, controlled damping

Table 4.1: Conditions for simulation

| Altitude | $\alpha_0$ | $\dot{\alpha_0}$ | Cg position | Control |
|---|---|---|---|---|
| 150 km | $45^o$ | $0^o/s$ | 30% from nose | $k_d = 1e-4, k_p = 0$ |

## 4.3 Considerations of damping time

It is desirable for a vehicle to dissipate its oscillatory motion as rapidly as possible, to provide the mission a maximum amount of time in a science-collection attitude. The variables available to mission designers include the overall pointing requirement, the altitude altitude at which the dissipation occurs, the overall mass of the CubeSat, and the cg position within the CubeSat.

Figure 4.2 shows the required torque magnitude versus desired time to threshold for various desired

pointing requirements, for a CubeSat at 150 km with a cg position of 30% of spacecraft length. It is unsurprising to note that less-stringent pointing requirements are met with less required torque for the same time to threshold. From this analysis, it appears that the difference between a $10^o$ and a $2^o$ pointing requirement, for the same torque magnitude, is on the order of 500 seconds. For a 150 km altitude orbit, the period is approximately 5,300 seconds (87.5 minutes), meaning that at this altitude even the $1 \times 10^{-5}$ N-m case is able to damp the motion in one orbit.

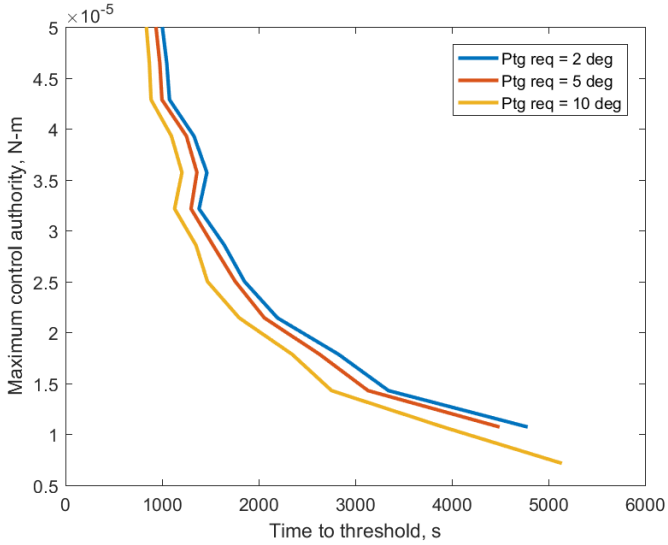


Figure 4.2: Required torque magnitude vs. desired damping time for various pointing accuracy requirements, h = 150 km, cg @ 30%.

Figure 4.3 shows the same torque vs. time curve as above for various altitudes, when considering a CubeSat with 30% cg position and pointing requirement of $5^o$. It appears there is almost no correlation between the altitude at which the dissipative action occurs and the time required to perform the maneuver. Therefore there is no altitude dependence on when the vehicle's motion is easier to damp, so it should occur as soon as possible in the mission profile to maximize the time spent in science collection attitude.

Figure 4.4 shows the effect of changing the cg position on the torque vs time curve. A further-aft cg position appears to ease the torque required for a set time to threshold. This is likely due to the decreased amplitude of torque on the spacecraft, causing the CubeSat to have a slower oscillation. Similarly, Figure 4.5 shows that a decreased total mass of the system decreases the required torque amplitude. This is likely due to the decreased moment of inertia of the spacecraft allowing the control system to accelerate the vehicle more readily. Because CubeSats are already so mass-constrained, this is an unfortunate finding.

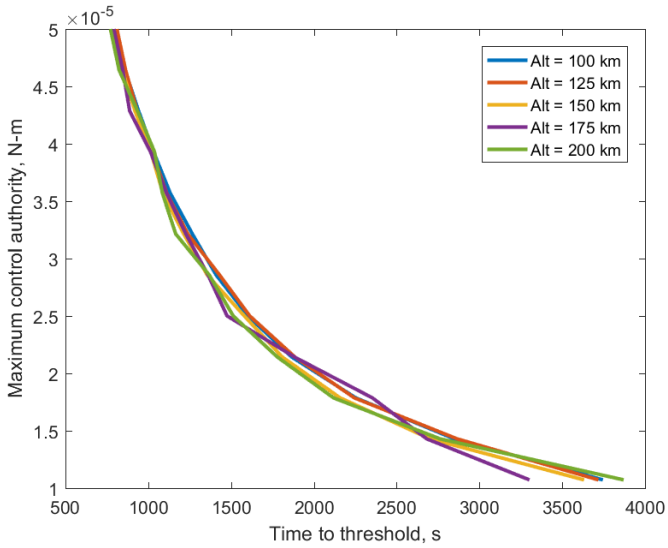


Figure 4.3: Required torque magnitude vs. desired damping time for various altitudes, threshold = $5^o$, cg @ 30%.

## 4.4 Noncircular Orbits

A CubeSat atmospheric probe will not likely be placed on a circular orbit upon jettison from its host. The effect of a noncircular orbit is a time-varying atmospheric density and velocity, and thus a changing magnitude of aerodynamic forces. These effects must be analyzed to ensure they will not adversely affect a mission.

Figure 4.6 shows the angle of attack and altitude time history for an uncontrolled CubeSat in a 150 x 200 km altitude orbit, initial angle of attack of $45^o$, and cg position of 30% spacecraft length. The oscillations begin in the 150 km region, and appear to stay in the initial range for the first half-wavelength of the oscillation. However, as the CubeSat rises in altitude, and correspondingly the aerodynamic forces decrease, it experiences a decreased restorative torque as it swings upward past trim. This reduced torque causes it to overshoot the initial angle of attack, up to nearly $80^o$. It then begins swinging back down to trim as it begins lowering in altitude. The descending altitude again increases the magnitude of the aerodynamic forces, causing the restorative torque to increase as the CubeSat swings below trim again, causing its maximum angle of attack to reduce back to roughly its initial amplitude. This trend then continues for the next few orbits, indicating this is a stable oscillation.

Adding control to this noncircular orbit behaves similarly to the circular orbit cases, wherein the oscillatory motion is damped within an orbit, as seen in Figure 4.7. However, there is a sensitivity to the eccentricity of the orbit, as shown in Figure 4.8. The same control gain is used in this case as in Figure

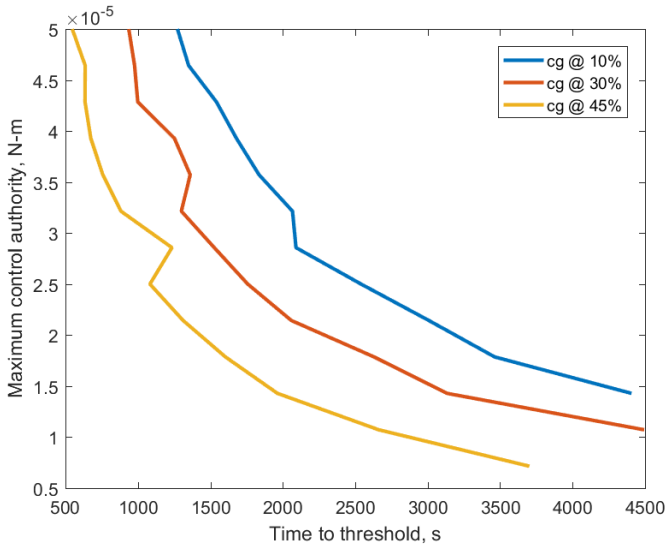


Figure 4.4: Required torque magnitude vs. desired damping time for various cg positions, threshold = $5^o$, h = 150 km.

4.7, however the CubeSat rises to a much higher altitude in this case. The CubeSat enters into a situation where the local aerodynamics are much less than the available torquing capability, causing it to overpower the aerodynamics and reach a nearly stationary condition at approximately $25^o$. It then moves deeper into the atmosphere again and moves closer to the trim condition, beginning a trend of ringing followed by a gentle rise, followed by more ringing. This undesirable behavior would be alleviated by gain scheduling.

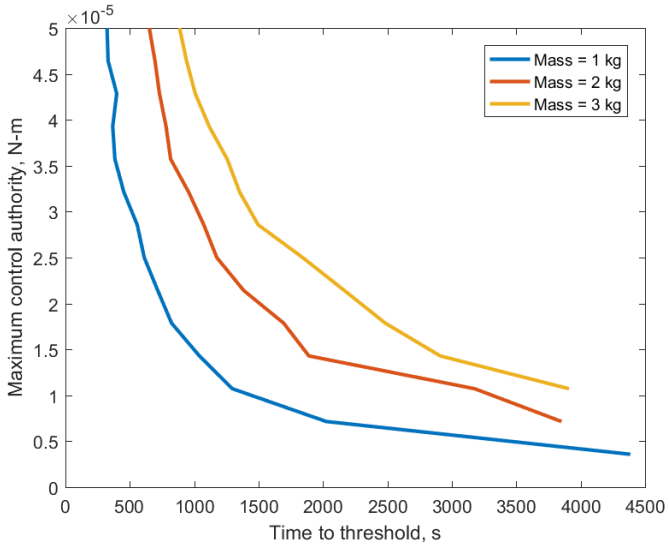


Figure 4.5: Required torque magnitude vs. desired damping time for various total masses, threshold = $5^o$, h = 150 km, cg @ 30%.

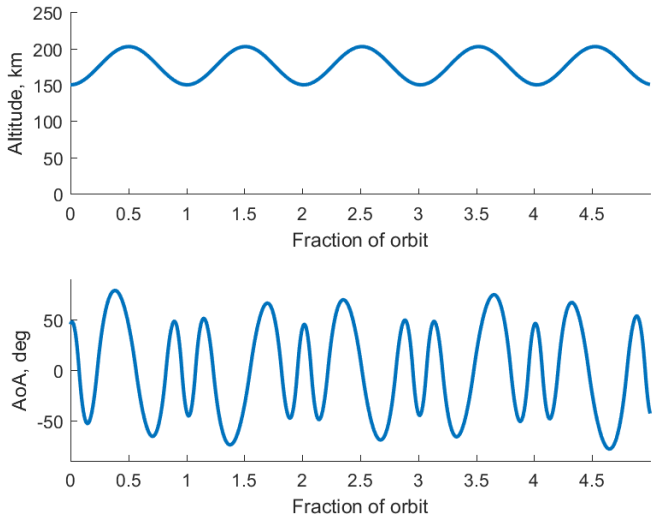


Figure 4.6: Time history of Angle of Attack and altitude for a noncircular orbit without control. $\alpha_0 = 45^o$, cg @ 30%

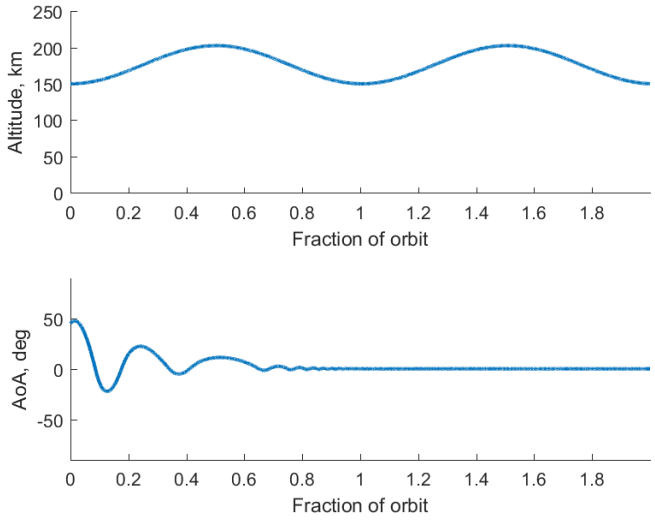


Figure 4.7: Time history of Angle of Attack and altitude for a noncircular orbit with control. $\alpha_0 = 45^o$, cg @ 30%, $k_d = 1 \times 10^{-4}$

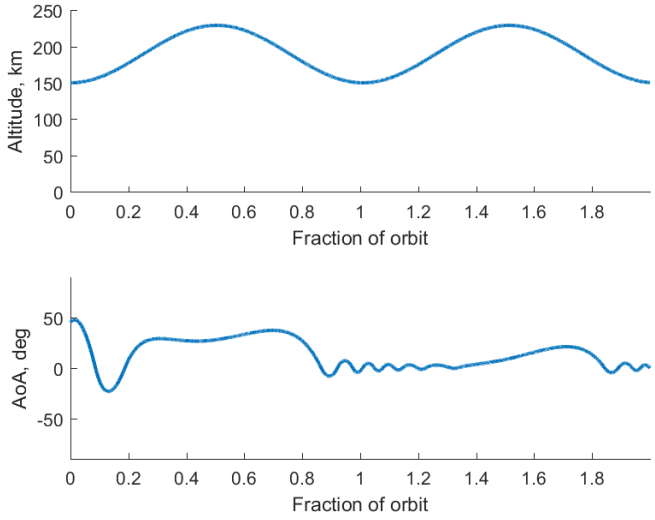


Figure 4.8: Time history of Angle of Attack and altitude for a noncircular orbit with control, but with a higher apoapsis. $\alpha_0 = 45^o$, cg @ 30%, $k_d = 1 \times 10^{-4}$

# Chapter 5

# Conclusions

This thesis presents analysis concerning the aerodynamic stability of a 3-U CubeSat in high-speed rarefied flow. The effects of the atmosphere may begin to overpower the control authority of a CubeSat as it descends below 200 km altitude. It is important that the vehicle be aerodynamically stable in this regime of flight to prevent premature mission termination.

A center of gravity of the vehicle that is fore of the neutral point provides a negative pitching moment coefficient. This leads to a restorative torque being created, causing the vehicle to oscillate around its trim point. There is a lack of appreciable aerodynamic damping in this high-speed, rarefied flow due to the lack of viscous forces and the minuscule effect of angular rate on the local angle of attack. A simple derivative control scheme using the vehicle's control system can serve to damp out oscillations on timescales less than a single orbit.

The density of the atmosphere increases as the vehicle descends in altitude, leading to increased aerodynamic forces and therefore increased resultant angular rates. Similarly, a further-fore cg position creates a larger torque for a similar state. This larger torque is balanced by the slightly increased moment of inertia, but the net effect is larger angular rates. Cg positions aft of the neutral point cause the trim condition to be an angle of attack of $180^o$, which is an undesirable effect.

A vehicle at zero angle of attack and zero angular rate will have an induced angle of attack which then causes a small oscillation around the trim point. This induced motion is larger in amplitude at higher altitudes due to the lower torques produced by the atmosphere. At lower altitudes, this small natural oscillation is on the order of common pointing requirements, leading to the possibility of switching the control system off during this condition.

General trends are inferred from the data available. High torque capability mixed with a moderately-forward cg position leads to a stable vehicle with minimal required time to damp oscillations to a specified threshold. The altitude at which this control occurs does not affect the time required, so active control should be performed as soon as possible from a mission design perspective. Higher-mass systems appear to require more torque capability to damp in similar times. Non-circular orbits complicate the motion and

required control scheme of the vehicle, but do not appear to adversely affect the motion of the vehicle more than circular orbits.

# Chapter 6

# References


[1] Darrin, A. and O'Leary, B., *Handbook of space engineering, archaeology, and heritage*, chap. 6, CRC Press, 2009, pp. 83–85.

[2] Pisacane, V., *The Space Environment and Its Effects on Space Systems*, chap. 7, American Institute of Aeronautics and Astronautics, 2008, pp. 170–173.

[3] Zuiker, N. et al., "Design of a CubeSat Mission to Investigate High-Enthalpy Noneqilibrium Flow Chemistry," 2018.

[4] Bailet, G., Sakraker, I., Scholz, T., and Muylaert, J., "Qubesat for Aerothermodynamic Research and Measurement on AblatioN," 2012.

[5] Morgan, J. et al., "Prediction of Flight Measurements of High-Enthalpy Nonequilibrium Flow from a CubeSat-Class Atmospheric Probe," *2018 AIAA Aerospace Sciences Meeting*, 2018, pp. 1–29.

[6] Palmerini, G., Sgubini, S., and Taini, G., "Spacecraft Orbit Control using Air Drag," *56th International Astronautical Congress of the International Astronautical Federation, the International Academy of Astronautics, and the International Institute of Space Law*, 2005, pp. 1–8.

[7] Turansky, C. P. and Argrow, B. M., "Rigid-Body Dynamics in Free-Molecular and Transition Flow," *Journal of Spacecraft and Rockets*, Vol. 51, No. 1, 2014, pp. 239–252.

[8] Turansky, C. P. and Argrow, B. M., "Nonlinear Dynamics of Objects in Transition Flow During Atmospheric Entry," *Journal of Spacecraft and Rockets*, Vol. 51, No. 3, 2014, pp. 855–872.

[9] Stalder, J. and Zurick, V., "Theoretical Aerodynamic Characteristics of Bodies in a Free-Molecule-Flow Field," 1951.

[10] Tsien, H.-S., "Superaerodynamics, mechanics of rarefied gases," *Journal of the Aeronautical Sciences*, Vol. 13, No. 12, 1946, pp. 653–664.

[11] Ashley, H., "Applications of the Theory of Free Molecule Flow to Aeronautics," *Journal of the Aeronautical Sciences (Institute of the Aeronautical Sciences)*, Vol. 16, No. 2, 1949, pp. 95–104.

[12] Glover, L. and Hagan, J. C., "The motion of ballistic missiles," *Technical memorandum*, , No. 8, 1971.

[13] Hughes, S. P., Qureshi, R. H., Cooley, S. D., and Parker, J. J., "Verification and Validation of the General Mission Analysis Tool (GMAT)," *AIAA/AAS Astrodynamics Specialist Conference*, , No. August, 2014.

[14] Analytical Graphics, I., "STK - Modeling Drag," 2018.

[15] Plimpton, S. and Gallis, M., "SPARTA Direct Simulation Monte Carlo (DSMC) Simulator," 2018.

[16] Schaaf, S. and Chambre, P., *Flow of Rarefied Gases*, Vol. 8, chap. H, Princeton University Press, Princeton, New Jersey, 1961.

[17] Koppenwallner, G. and Legge, H., "Drag of Bodies in Rarefied Hypersonic Flow," *Thermophysical Aspects of Reentry Flows*, 1986, pp. 44–59.

[18] Boyd, I. D., Phillips, W. D., and Levin, D. A., "Prediction of Ultraviolet Radiation in Nonequilibrium Hypersonic Bow-Shock Waves Introduction," *Journal of Thermophysics and Heat Transfer*, Vol. 12, No. 1, 1998, pp. 38–44.

[19] Anderson, J. D., *Hypersonic and High-Temperature Gas Dynamics*, chap. 3, American Institute of Aeronautica and Astronautics, Inc., 2006, pp. 57–58.

[20] Nelson, R., *Flight Stability and Automatic Control*, chap. 1, 2, The McGraw-Hill Companies, Inc., 1998, pp. 19–22, 42–44.

[21] Papitashvili, N., "MSIS-E-90 Atmosphere Model," 2018.

[22] Etkin, B., *Dynamics of Atmospheric Flight*, chap. 4, 5, Dover Publications, Inc., 2000, pp. 104–144.

[23] Ginsberg, J., *Advanced Engineering Dynamics*, chap. 3, 4, 5, CRC Press, 2009, pp. 56–203.

[24] Wertz, J. and Larson, W., *Space Mission Analysis and Design*, chap. 11, Microcosm Press, 1999, pp. 371–376.

[25] Pikus, A. et al., "DSMC Aerothermal Study for 3U CubeSat Probes in LEO," *AIAA Aviation Forum*, 2017.

[26] Wiesel, W., *Spaceflight Dynamics*, chap. 6, Aphelion Press, 2010, pp. 199–204.